

1 **Revision 1:**

2

3 **Nanostructure reveals REE mineral crystallization mechanisms in**
4 **granites from heavy-REE deposit, South China**

5

6 AIGUO SHI¹, CHENG XU^{1,2*}, ANTON R. CHAKHMOURADIAN³, MARTIN P.
7 SMITH⁴, JINDRICH KYNICKY⁵, CHAOXI FAN¹, CHUNWAN WEI¹, GUANGXI
8 KUANG¹

9 ¹Key Laboratory of Orogenic Belts and Crustal Evolution, School of Earth and
10 Space Sciences, Peking University, Beijing 100871, China.

11 ²College of Earth Sciences, Guilin University of Technology, Guilin 540001,
12 China.

13 ³Department of Geological Sciences, University of Manitoba, Winnipeg, MB
14 R3T2N2, Canada.

15 ⁴School of Environment and Technology, University of Brighton, Brighton
16 BN24GJ, UK.

17 ⁵BIC Brno, Technology Innovation Transfer Chamber, Brno 61200, Czech
18 Republic.

19

20

21 *Email: xucheng1999@pku.edu.cn

22

23

ABSTRACT

24 Weathering crusts after granites are the most important source of heavy
25 rare-earth elements (HREE) worldwide. Although HREE in these deposits are
26 known to be inherited from parental rocks, the origin of HREE enrichment and
27 reasons why it is rare outside of China remain unclear. Here, we report the
28 occurrence of variably organized nanoparticles of Ce-poor (<0.2 wt.%),
29 Nd-Y-rich bastnäsite-(La) and associated cerianite in parental granites from a
30 HREE deposit, South China. The mineral contains high HREE abundances (up
31 to 13 wt.% Y_2O_3). Synchrotron radiation-induced X-ray diffraction and
32 high-resolution transmission electron microscopy analyses suggest that the
33 mineral grew as disordered nanocrystals, and coaligned, or nearly coaligned
34 nanoparticle aggregations, thus supporting “nonclassical” crystallization
35 mechanisms by particle attachment under hydrothermal conditions. The
36 nanocrystalline Ce-poor, Nd-Y-rich bastnäsite-(La) precipitated at rapidly
37 decreasing temperature related to the influx of externally derived fluids, which
38 caused CO_2 - H_2O immiscibility and REE supersaturation. This interpretation is
39 supported by petrographic data and microthermometric analysis of fluid
40 inclusions in quartz. Unusually high $f(O_2)$ resulted in Ce oxidation and
41 decoupling from trivalent lanthanides, producing polycrystalline mineralization,
42 which decomposed easily during late weathering stages to release HREE.

43 **Keywords:** Ce-poor and Nd-Y-rich bastnäsite-(La), nanoparticles,
44 crystallization by particle attachment, oxygen fugacity, REE deposits, South
45 China granite

46

47

INTRODUCTION

48 The rare-earth elements (REE), generally defined as the lanthanides plus
49 yttrium (Y), are considered critical raw materials because of their extensive
50 applications in renewable energy solutions and modern technologies (Kalvig
51 and Machacek 2018). Recently, concerns over the perceived imbalance
52 between the increasing demand for these resources and their supply
53 shortages have led to a surge in REE exploration worldwide, since China, the
54 largest REE producer in the past 30 years, reduced its REE export quota
55 (Gulley et al. 2018). Heavy REE (HREE = Gd-Lu + Y) are much less abundant
56 than light REE (LREE = La-Eu) and are anticipated to be associated with the
57 highest supply risk in the foreseeable future (Balaram 2019). The majority of
58 economically exploitable HREE resources are associated with regolith-hosted
59 ion-adsorption deposits (IAD) in South China (Martin et al. 2020). The HREE
60 are adsorbed as ionic complexes onto clay minerals in weathering crusts
61 developed over igneous, mostly granitoid rocks (Bao et al. 2008). These
62 deposits account for about 80% of the global HREE supply (Bernhardt and
63 Reilly 2020). The forms of REE adsorption on clays reported to date primarily

64 include readily leachable eightfold- to ninefold-coordinated outer-sphere
65 hydrated complexes, dominantly attached to the clays kaolinite and halloysite
66 (Borst et al. 2020). Although weathering of granitoids under warm and humid
67 conditions plays an important role in REE fractionation and enrichment, this
68 process is expected to yield high LREE/HREE ratios in IAD because LREE are
69 hosted in phases relative more susceptible to weathering in comparison with
70 HREE-enriched phases (Estrade et al. 2019; Prameswara et al. 2021).
71 Geologically similar IAD were identified elsewhere in Southeast Asia
72 (Sanematsu et al. 2013) and Madagascar (Janots et al. 2015), and these
73 deposits generally exhibit stronger enrichment in LREE than HREE. The
74 extent of relative enrichment and fractionation among leachable REE is
75 believed to be controlled by the nature of precursor bedrock and REE-hosting
76 minerals in that rock (Martin et al. 2017; Estrade et al. 2019). Therefore, one
77 essential question that needs to be addressed to understand the origin of IAD
78 is how HREE-rich minerals form in their precursor granitoid rocks.

79 Xu et al. (2017) reported three types of previously unidentified, Ce-poor,
80 LREE- and HREE-enriched minerals in the South China granites. The
81 weathering profiles inherited the REE signature of their parental granites,
82 reflecting the depletion in Ce and enrichment in both LREE and HREE.
83 Different horizons within the weathering profile show variable enrichment
84 levels in LREE and HREE. Uncommon REE minerals were interpreted to have

85 served as the principal source of HREE incorporated in the mineralized
86 weathering crusts (Xu et al. 2017); however, the exact nature and genesis of
87 these minerals were not very clear. Understanding their origin and paragenetic
88 role in the parental granites has become a priority in explaining why HREE-rich
89 clays are particularly abundant in South China. This work also has practical
90 implications for mineral exploration as it provides criteria for the identification of
91 similar HREE-rich IAD elsewhere. Here, we report unusual nanostructures
92 observed in a Ce-poor, REE fluorocarbonate mineral [referred to hereafter as
93 Ce-poor, Nd-Y-rich bastnäsite-(La)] from the Zhaibei granites, which
94 weathered to give rise to the famous HREE deposits of South China (also
95 known as “South China clays”). Our results provide evidence for a
96 crystallization mechanism novel among REE minerals, which involves crystal
97 growth by oriented and disoriented attachment of nanoparticles, and further
98 supports the idea that HREE enrichment in the parental granites was related to
99 rapid crystallization in a highly oxidized environment.

100

101

GEOLOGICAL BACKGROUND

102

103

104

105

Vast quantities of granitic rocks, associated with subordinate gabbros and basalts, were emplaced in the South China Block during the Mesozoic. Mao et al. (2008) suggested that these rocks were products of three episodes of magmatic activity: Late Triassic (230-210 Ma), Middle-Late Jurassic (170-150

106 Ma) and Early Cretaceous (134-90 Ma). The Early Mesozoic intrusions were
107 confined mostly to intracontinental areas, whereas the Cretaceous granites
108 were distributed mainly towards the South China Sea coast (Fig. 1). Many
109 studies identified subduction of the Paleo-Pacific plate beneath the Eurasian
110 plate as responsible for the Mesozoic granitic magmatism in the region (Li and
111 Li 2007; Zhou et al. 2006; Zhou et al. 2015). The Triassic episode produced
112 voluminous S-type granites with high modal contents of Al silicates, in
113 particular muscovite, garnet and tourmaline (Wang et al. 2013). Jurassic
114 granites are widespread in the Nanling region and primarily composed of
115 biotite and two-mica varieties. These rocks include calc-alkaline I-type, alkaline
116 A-type and subordinate S-type granites (Zhou et al. 2015). Cretaceous
117 granites are mostly of A- and I-types, and tend to occur closer to the coast
118 (Sun et al. 2015).

119 Ore deposits are quite abundant in the South China granitic belt and
120 include W, Sn, Sb, Bi, Cu, Pb, Zn, Nb, Ta and REE targets. More than 90% of
121 the HREE-rich IAD are located in Jiangxi, Guangdong and Guangxi provinces
122 (Fig. 1). The examined weathering profiles in Zhaibei, southern Jiangxi, have a
123 thickness ranging from 5 to 30 m, and are developed after Middle-Jurassic
124 peraluminous biotite and muscovite granites (Li et al. 2003; Wang et al. 2015).
125 The mineralized laterites show moderate LREE enrichment levels and
126 negative Ce and Eu anomalies; their REE budget (215-1334 ppm) is made up

127 of ~30-50% HREE (57-542 ppm; Xu et al. 2017). The Jurassic (188 Ma; Xu et
128 al. 2017) granites intruding Paleozoic granitoids have intrusive contacts with
129 Jurassic volcanic rocks in the western part of the study area, and are
130 separated by a fault from Cambrian metamorphic rocks in its northern part.
131 The parental rock of the Zhaibei REE-rich clays is medium- to coarse-grained
132 and composed of alkali feldspar (25-30%), plagioclase (25-32%), quartz
133 (30-35%), biotite (3-10%) and muscovite (< 2%) (Online Material¹ Fig. S1). The
134 accessory mineral assemblage includes REE phases, zircon, fluorapatite,
135 magnetite and ilmenite. The REE minerals are represented by monazite-(Ce),
136 xenotime-(Y), Ca-REE fluorocarbonates, allanite-(Ce), cerianite-(Ce) and
137 three HREE-rich minerals described in our earlier work as “REE-1, 2, 3”. Both
138 REE-1 and REE-2 apparently formed by alteration of fluorapatite, which is
139 highly susceptible to fluid-induced chemical and textural changes under
140 natural and experimental conditions (Fig. 2a; Harlov and Förster 2003; Harlov
141 2015; Chakhmouradian et al. 2017). The Ce-poor, Nd-Y-rich bastnäsite-(La)
142 (“REE-3”) occurs as fracture fillings in feldspar and disseminated anhedral
143 grains up to 200 μm in size developed interstitially to quartz, biotite and
144 feldspar (Fig. 2b, c). Cavernous samples contain thin encrustations of Ce-poor,
145 Nd-Y-rich bastnäsite-(La) lining cavities (Fig. 2c). The mineral did not form at
146 an early stage of the weathering event, and is in direct contact with biotite,
147 quartz and feldspar, or separated from them by a rim of unidentified hydrous

148 Al-Fe-rich silicate (Fig. 2c, d) in the fresh parental rock. The cerianite veinlets
149 are observed in the granite, where they are intimately intergrown with an
150 unidentified hydrous Al-Fe-rich silicate (Fig. 2e). Ilmenite in this granite was
151 partially converted to hematite, which was confirmed by Raman
152 microspectroscopy (Fig. 2f and Online Material¹ Fig. S2).

153

154

ANALYTICAL METHODS

155 **Mineral analysis**

156 The major-element compositions of mineral phases in the granites were
157 analyzed by wavelength-dispersive X-ray spectrometry (WDS) using a JEOL
158 JXA-8230 electron microprobe at the East China University of Technology.
159 According to the chemical composition and grain size of individual minerals,
160 each of them was analyzed with a set of appropriate matrix-specific standards
161 (both natural and synthetic) and optimized instrumental conditions (detector
162 type, beam settings and counting statistics). The standards used during for the
163 WDS analyses included sanidine (Si, K), plagioclase (Ca), rutile (Ti), magnetite
164 (Fe), rhodonite (Mn), fluorite (F), jadeite (Na, Al), apatite (P), biotite (Mg),
165 metallic Nb and Ta (Nb, Ta), uraninite (Th, U, Pb), monazite (La, Ce, Pr, Nd),
166 and synthetic REE phosphates (Y, Sm, Eu, Gd, Dy, Ho, Er, Tm, Yb). The
167 measurements were performed at an accelerating voltage of 15 kV and a
168 beam current of 20 nA, with an electron beam ranging 1-5 μm in diameter. For

169 the analysis, K α analytical lines were used for all elements except La, Ce, Pr,
170 Nd, Nb and Ta (L α lines for all), and Sm (L β line). For REE-bearing minerals,
171 raw WDS data were corrected using empirical interference values for REE and
172 other elements potentially interfering with the REE signals, determined for
173 the well-characterized synthetic glass and phosphate standards. All raw data
174 were corrected with standard ZAF correction procedures. Repeated analysis of
175 the standards showed that precision of the WDS measurements was ± 2 % or
176 better for most elements.

177

178 **Synchrotron radiation-induced X-ray diffraction (SR-XRD)**

179 In-situ SR-XRD analysis of Ce-poor, Nd-Y-rich bastnäsite-(La) was
180 performed on polished thin sections at the 4W2 beamline of Beijing
181 Synchrotron Radiation Facility. The wavelength of the monochromatic X-ray
182 beam was 0.6199 Å and the beam size was 20 × 30 μm^2 . During the
183 measurement, the silicate minerals surrounding Ce-poor, Nd-Y-rich
184 bastnäsite-(La) were covered with a copper sheet with a hole 150 μm in
185 diameter, which is close to the size of analyzed fluorocarbonate grains. The
186 thin section was continuously rotated from -20° to 20° about the X-ray beam
187 axis at ambient conditions, and the collecting time was 300 s. The X-ray
188 diffraction (XRD) patterns were acquired using an image plate detector
189 (MAR-345), calibrated with a CeO₂ standard, and then integrated to generate

190 conventional one-dimensional profiles using the Fit2D program (Hammersley
191 1997).

192

193 **High-resolution transmission electron microscopy (HRTEM)**

194 Electron-transparent foils of representative Ce-poor, Nd-Y-rich
195 bastnäsite-(La) grains for HRTEM analysis were prepared by focused ion
196 beam technique (FIB, Online Material¹ Fig. S3) using a Zeiss Auriga Compact
197 dual beam instrument equipped with an Omniprobe AutoProbe 200
198 micromanipulator at the Institute of Geology and Geophysics, Chinese
199 Academy of Sciences. Final thinning and polishing were done using an ion
200 beam at a voltage of 5-30 kV and beam current of 0.05-2 nA. The FIB section
201 was ~100 nm in thickness. HRTEM images of the foils were obtained with an
202 aberration-corrected scanning transmission electron microscope (FEI Titan
203 Cubed Themis G2 300 at Peking University), which was operated at an
204 accelerating voltage of 300 kV and a beam current of ~2 nA. In addition,
205 high-angle annular dark-field (HAADF) scanning transmission electron
206 microscopy images and energy-dispersive X-ray spectroscopy (EDS) maps
207 were recorded at an accelerating voltage of 300 kV and beam currents of ~50
208 pA and ~100 pA, respectively (Rice et al. 1990). EDS analyses were done in
209 scanning transmission electron microscopy (STEM) mode to avoid mass loss
210 during data acquisition. High-resolution lattice fringe images were used to

211 calculate fast Fourier-transformed (FFT) patterns (Chen et al. 2020). The
212 measurement of *d*-spacings was performed with the Digital Micrograph
213 software.

214

215 **Fluid inclusion analysis**

216 Raman microspectroscopy was used to determine the composition (both
217 fluid and gas phases) of individual fluid inclusions and to identify different
218 mineral phases at ambient conditions. For this purpose, we employed a
219 HORIBA Jobin Yvon LabRAM HR Evolution confocal micro-Raman system
220 equipped with an Olympus microscope and a frequency-doubled Nd:YAG
221 green laser (532 nm) at Peking University (Cui et al. 2020). The micro-Raman
222 system is equipped with a 20× long-working distance objective (NA = 0.25),
223 and a stigmatic 800 mm spectrometer with a 1800 groove/mm diffraction
224 grating. The spectrometer was calibrated using a mirror-polished synthetic Si
225 standard. The laser power at the source was 100 mW. The confocal hole was
226 set at 500 μm and the corresponding spectral resolution was $\pm 0.7 \text{ cm}^{-1}$. The
227 laser beam was focused on fluid inclusions close to the upper surface of thin
228 sections and Raman spectra between 100 and 4000 cm^{-1} were recorded. Data
229 acquisition times for fluid inclusions varied between 30 s and 60 s depending
230 on the morphological and compositional characteristics of each inclusion and
231 its location. For mineral phases, Raman spectra between 100 and 1300 cm^{-1}

232 were recorded for 10 to 15 seconds and were checked against a common
233 standard database.

234 Microthermometric measurements were performed at Peking University
235 using a LINKAM THMS 600 heating-freezing stage operating in a temperature
236 range of -196 °C to +600 °C. Accuracy of the measurements was ensured by
237 calibration at -56.6 °C and 0 °C using synthetic fluid inclusion standards and
238 pure water. The measurement precision ranged from ± 0.1 °C between -120
239 and -70 °C, to ± 0.2 °C between -70 and 100 °C, and ± 1 °C between 100 and
240 600 °C. During each round of measurements, the temperature was first
241 decreased to -120 °C, and then gradually ramped up. The heating rate was
242 reduced to 0.2-0.5 °C min⁻¹ close to the phase transitions. Ice-melting
243 temperatures and total homogenization temperatures of fluid inclusions were
244 measured at a heating rate of 0.5 °C min⁻¹. Melting temperatures of solid CO₂
245 and clathrate, and homogenization temperatures of CO₂ phases were
246 observed at a heating rate of 0.2-0.5 °C min⁻¹. Salinities of the NaCl-H₂O
247 inclusions were calculated using the final ice-melting temperatures (Bodnar
248 1993). For tri-phase CO₂-rich inclusions (H₂O-NaCl-CO₂ system), salinities
249 were calculated using the clathrate melting temperatures in combination with
250 liquid-vapor equilibria (Bakker 1997). Program DENSITY and Chueh and
251 Prausnitz's (1967) equation of state were chosen for these calculations.

252

RESULTS

253

254 **Mineral chemistry**

255 Fresh granite samples comprise abundant K feldspar ($\text{Ab}_{2-6}\text{Or}_{94-98}$) and
256 plagioclase ($\text{An}_{2-10}\text{Ab}_{88-97}\text{Or}_{\leq 1}$) (where Ab, An and Or stand for the albite,
257 anorthite and orthoclase end-members, respectively). Minor albite is also
258 present as exsolution lamellae in K-feldspar. Biotite is a volumetrically
259 significant (up to 10 vol.%) constituent of these rocks, occurring as clusters of
260 platy crystals up to 4 mm across. It contains high FeO and TiO_2 contents
261 (29.8-31.1 and 3.1-3.7 wt.%, respectively) at low MgO levels (3.1-4.0 wt.%,
262 Online Material¹ Table S1). Some biotite crystals contain inclusions of “REE-1”
263 and “REE-2”, which correspond to REE-phosphates with high La_2O_3 and Y_2O_3
264 contents (4-12 and 10-51 wt.%, respectively; Xu et al. 2017). Both these
265 minerals are characterized by low Ce abundances, at or below its detection
266 limit by electron-microprobe analysis. Cerium-poor, Nd-Y-rich bastnäsite-(La)
267 is a fluorocarbonate containing <0.2 wt.% Ce. Its total REE content is high and
268 dominated by La, Nd and Y (up to 30.6, 20.7 and 12.9 wt.% respective oxides,
269 Table 1). To our knowledge, this mineral has not previously been reported in
270 the granites of South China, which generally contain normal bastnäsite-(Ce)
271 and parisite-(Ce) with high Ce but low Y abundances (20-30 wt.% and <4 wt.%
272 respective oxides: Wang et al. 2015; He et al. 2017; Martin et al. 2017). The
273 composition of cerianite could not be determined with accuracy because of its

274 intimate association with hydrous silicates (Online Material¹ Table S1).

275

276 **Ce-poor, Nd-Y-rich bastnäsite-(La) structural analysis**

277 The SR-XRD analysis of representative grains of Ce-poor, Nd-Y-rich
278 bastnäsite-(La) demonstrates that it is composed of randomly oriented crystals
279 (Fig. 3). The collected SR-XRD pattern consists of sharp and narrow diffraction
280 peaks, whose full-width-at-half-maximum values indicate particle sizes of <1
281 μm (Monshi et al. 2012). The measured d -spacings (1.137-4.847 Å) are close
282 to, but slightly smaller than, those of Y-poor bastnäsite-(La) (1.149-4.859 Å,
283 Online Material¹ Table S2), probably due to the relatively large proportion in
284 the La site of such small cations as Y^{3+} and heavy lanthanides.

285 Examination of the Ce-poor, Nd-Y-rich bastnäsite-(La) with high-resolution
286 transmission electron microscopy (HRTEM) reveals that its aggregates contain
287 very small crystallites ranging from 5 to 10 nm across (Fig. 4a). The acquired
288 nanoscale compositional maps (including C, O, F, La, Nd and Y) are uniform
289 and show no compositional variation whatsoever (Fig. 4b-g). The boundaries
290 between nanoparticles and larger grains, imaged by HRTEM (Fig. 5 and
291 Online Material¹ Fig. S4), show gradual transition from crudely aligned
292 nanoparticles to submicrometer-sized grains. The degree of crystallinity within
293 a specific region of the HRTEM foil is directly related to variations between
294 random and aligned aggregation states of the nanoparticles. Four

295 representative states have been recognized on the basis of the HRTEM
296 images (Fig. 6), described in further detail below.

297 The first type, represented by randomly aggregated nanoparticles, is
298 characterized by randomly oriented lattice fringes and diffraction rings in fast
299 FFT patterns (Fig. 6a). The aggregation state of Ce-poor, Nd-Y-rich
300 bastnäsite-(La) nanoparticles in this case is similar to that of some synthetic
301 examples produced by rapid crystallization: for example, poorly ordered Cu
302 oxalate (Soare et al. 2006) and akaganeite (Nielsen et al. 2014). The second
303 type of aggregates represents a mixture of randomly oriented and crudely
304 aligned nanoparticles (Fig. 6b). They are characterized by FFT patterns
305 featuring both diffraction spots and rings, indicative of ordered and disordered
306 aggregation, respectively. The third type shows parallelism of most lattice
307 fringes and FFT patterns comprising mostly diffraction spots with some fuzzy
308 diffraction rings (Fig. 6c). These features demonstrate that most of the
309 nanoparticles are aligned, although some misoriented lattice fringes indicate
310 that the process of re-arrangement and recrystallization to eliminate the
311 imperfections of initial aggregation has not finished yet (De Yoreo et al. 2015).
312 In the fourth type of aggregates, nanoparticles are assembled into
313 submicrometer-sized crystallites showing well-defined diffraction patterns (Fig.
314 6d). Notably, adjacent crystals are separated from one another by areas
315 composed of disordered nanoparticles, indicating that oriented aggregation

316 initiated at multiple sites simultaneously (Banfield et al. 2000). The
317 polycrystalline nature of Ce-poor, Nd-Y-rich bastnäsite-(La) suggests that the
318 orientation adopted by one crystal is unrelated to those of adjacent crystals.
319 Atomic plane spacings of about 2.0, 2.9, 3.3, 3.6 and 4.8 Å were observed in
320 lattice fringe images (Fig. 6) and show reasonable agreement with the values
321 measured by SR-XRD (2.0, 2.8, 3.3, 3.5 and 4.8 Å; Online Material¹ Table S2).

322

323 **Fluid inclusions**

324 Two main types of fluid inclusions were recognized in quartz adjacent to
325 the Ce-poor, Nd-Y-rich bastnäsite-(La) (Fig. 7 and Online Material¹ Fig. S1)
326 using Raman microspectroscopy: CO₂-H₂O-dominated and pure H₂O. The
327 CO₂-H₂O inclusions are pervasive and occur both as primary and secondary
328 inclusions forming a compact three-dimensional network and confined to
329 healed fractures. The gas/liquid filling ratio of these inclusions varies widely
330 (Fig. 7a). Two subtypes were distinguished among them. Subtype IA includes
331 three-phase inclusions (Fig. 7b) with an aqueous fluid, liquid CO₂ (20-60 vol.%
332 of the inclusion), and CO₂ gas (10-25 vol.% of the inclusion). The melting
333 temperature of the CO₂ phase in these inclusions ranges from -57.2 to
334 -58.3 °C. Clathrate melting temperatures range from 3.5 to 8.2 °C,
335 corresponding to salinities of 3.2-11.6 wt.% NaCl equivalent (Bakker 1997).
336 These inclusions mostly homogenized to an aqueous phase between 307 and

337 372 °C, and to a gas phase between 349 and 386 °C (Table 2). Subtype IB is
338 represented by CO₂-rich two-phase inclusions composed of an aqueous fluid
339 and a gas bubble, whose volume accounts for 20-70 % of the inclusion. Small
340 daughter crystals of calcite were also observed in some cases (Fig. 7c). The
341 pure H₂O inclusions of Type II are interpreted as secondary in origin (Fig. 7d).
342 The melting temperatures of ice were measured to range between -4.8 and
343 -7.3 °C, indicating low salinity values from 7.6 to 10.9 wt.% NaCl equivalent
344 (Bodnar 1993). These inclusions homogenize to a liquid phase between 168
345 and 347 °C (Table 2).

346

347

DISCUSSION

348 **Crystallization by particle attachment under REE supersaturation**

349 The classical nucleation theory, including terrace-ledge-kink and
350 dislocation growth models, has served as the prevalent conceptual basis for
351 describing crystal nucleation and growth since the 1950s (Burton et al. 1951;
352 Kashchiev 2003). However, in the past 30 years, an increasing number of
353 studies have provided convincing evidence for crystallization by particle
354 attachment (CPA) (Penn and Banfield 1999; Zhang et al. 2010; Li et al. 2012;
355 Boneschanscher et al. 2014; De Yoreo et al. 2015). The classical theory works
356 well for the precipitation of low-solubility phases from dilute solutions, but it is
357 not applicable at high degrees of supersaturation (Ivanov et al. 2014).

358 Thermodynamically, the nucleation energy barrier and critical nucleus size
359 should decrease with progressive deviation of the system from equilibrium –
360 for example, due to supersaturation (Ivanov et al. 2014). At low degrees of
361 supersaturation, crystals are expected to grow in accord with the classical
362 nucleation theory because the free-energy barrier is still relatively large
363 (Kashchiev 2003; Wallace et al. 2013). At high levels of supersaturation, the
364 free energy barrier is comparable with thermal energy, and nuclei may be
365 generated in sufficiently large numbers at multiple sites so as to counteract
366 supersaturation (Bray 2002; Scheifele et al. 2013). The particle density will
367 reach a level where a high particle collision rate will facilitate crystal growth by
368 CPA (Cölfen and Antonietti 2008).

369 Multiple intermediate states of atom-to-crystal evolution have been
370 recognized, from simple ions to bulk crystals assembling together by CPA, and
371 involving multi-ionic complexes, oligomers and nanoparticles (De Yoreo et al.
372 2015). Recent experiments showed that atoms in nanoscale nuclei (clusters of
373 ordered atoms or ionic groups) may fluctuate reversibly between ordered and
374 disordered states (Jeon et al. 2021). Similarly, fast crystal growth by CPA does
375 not always lead to a well-formed single crystal, but to an aggregate of slightly
376 misaligned domains (Huang et al. 2004; Soare et al. 2006; Nielsen et al. 2014).
377 Such nanoscale misalignment can be eventually eliminated by reaction with a
378 solution to reduce surface energy (Huang et al. 2004; Nielsen et al. 2014).

379 We postulate that crystals of Ce-poor, Nd-Y-rich bastnäsite-(La) in the
380 Zhaibei granites developed from initially disordered nanocrystals that
381 assembled into submicrometer-sized particles through CPA (Fig. 6). The
382 examined grains formed aggregates and were not re-arranged to form discrete,
383 structurally uniform single crystals. This indicates that the Ce-poor, Nd-Y-rich
384 bastnäsite-(La) precipitated rapidly from a supersaturated solution, but did not
385 undergo subsequent recrystallization.

386

387 **REE mineralization under highly oxidized conditions**

388 Supersaturation reported for natural aqueous systems is usually related to
389 microbial activity (Banfield et al. 2000; Penn et al. 2001). However, the
390 temperature of fluids responsible for the REE enrichment in the Zhaibei
391 granites is too high (~170-390 °C) for any microorganism to survive (Brock
392 1985). Notably, CO₂-rich and aqueous fluid inclusions commonly coexist in
393 these rocks. The gas/liquid volume ratio in such inclusions is variable, but their
394 homogenization temperatures are similar, suggesting CO₂-H₂O immiscibility in
395 their parental fluid (Yardley and Bottrell 1988). The loss of a low-salinity,
396 CO₂-rich phase would increase the pH value of the residual fluid, reduce
397 carbonate activity and increase solute concentrations in the H₂O-dominant
398 fraction (Bowers and Helgeson 1983). Thus, CO₂-H₂O immiscibility should
399 lead to REE supersaturation in the aqueous phase, triggering precipitation of

400 such low-solubility phases as cerianite and REE fluorocarbonates (Xiong 2015;
401 Migdisov et al. 2016). The very different Nd isotopic signature of Ce-poor,
402 Nd-Y-rich bastnäsite-(La) [$\epsilon\text{Nd}_{(t)} = 0.9 \pm 0.8$] in comparison with primary
403 monazite and apatite [$\epsilon\text{Nd}_{(t)} = -11.5 \pm 0.5$] in the parental granite (Xu et al.
404 2017) indicates an external fluid contribution. Although its source has not been
405 ascertained yet owing to the lack of isotopic data for other rock types in the
406 study area, the addition of an externally derived fluid would have certainly
407 resulted in rapid cooling of the hydrothermal system (Carrigan 1986). Thus, we
408 hypothesize that a sudden drop in temperature promoted $\text{CO}_2\text{-H}_2\text{O}$
409 immiscibility and ultimately triggered the precipitation of Ce-poor, Nd-Y-rich
410 bastnäsite-(La) nanoparticles at multiple nucleation sites. The CPA
411 documented in the present work occurred under moderate-temperature
412 hydrothermal conditions, in contrast to the previously reported cases in
413 synthetic, biogenic and low-temperature geological environments (Banfield et
414 al. 2000; Penn et al. 2001; Hochella et al. 2005), or rapidly quenched melt
415 pockets in Martian meteorites (Zhang et al. 2019).

416 The studied Ce-poor, Nd-Y-rich bastnäsite-(La) is characterized by high
417 LREE and HREE levels, but extremely low Ce contents. The presence of
418 cerianite and hematitization of ilmenite (Fig. 2f) indicate a high- $f\text{O}_2$ regime. The
419 oxidation of Ce^{3+} to Ce^{4+} is clearly responsible for the observed fractionation
420 between Ce^{4+} and larger and more mobile REE^{3+} cations; e.g., $^{138}\text{La}^{3+}$ is 18%

421 larger than $^{87}\text{Sr}/^{86}\text{Sr}$ (Shannon 1976). Owing to the low solubility of CeO_2 in fluids
422 (Xiong 2015), cerianite was precipitated as veinlets associated with the
423 hydrous Al-Fe-rich silicate mineral (Fig. 2e). The $\log f\text{O}_2$ values of Jurassic to
424 Early Cretaceous granites in South China range from -0.83 to +4.22 relative to
425 the NNO buffer (Li et al. 2017), which is too low for Ce oxidation (Burnham and
426 Berry 2014). The possible sources of oxidizing components could be incursion
427 of external fluids into granites at the subsolidus stage, derived either from
428 dehydrated lithospheric material, which subducted beneath the amalgamated
429 China continent in the early Jurassic (Liu et al. 2017), or from meteoric sources.
430 The $f\text{O}_2$ levels in arc magmas are estimated to be insufficient for Ce oxidation
431 (Kelley and Cottrell 2012; Burnham and Berry 2014). Incursion of meteoric
432 water into the subsolidus granites could result in high $f(\text{O}_2)$ values and
433 oxidation of Ce^{3+} to Ce^{4+} while not affecting the rest of the REE budget. This
434 process could have triggered a rapid temperature drop and the precipitation of
435 nanocrystalline HREE-rich carbonates with strong Ce depletion.

436 The poly-crystalline Ce-poor, HREE-rich minerals with a poorly-ordered
437 structure and numerous defects and dislocations are readily decomposed
438 during weathering (Wilson 2004), resulting in REE removal from the precursor
439 granite. Aqueous complexes can readily fractionate HREE from LREE during
440 intense weathering. In particular, HREE form stronger complexes with
441 carbonate and fluoride ligands than LREE at ambient temperature (Wood

442 1990), thereby increasing the concentration of the former in the fluid and
443 promoting their transport and adsorption onto clay minerals. This mechanism
444 may explain the anomalous HREE enrichment of some South China IAD.

445

446

IMPLICATIONS

447 The detailed HRTEM study of Ce-poor, Nd-Y-rich bastnäsite-(La)
448 presented above documented several successive steps in the aggregation of
449 nanoparticles to form submicrometer-sized crystallites. The observed
450 morphological evolution is best explained by CPA under supersaturated
451 conditions, as there is no HRTEM evidence for crystal-growth by terrace or
452 dislocation-constrained mechanisms. Cerium oxidation and its decoupling from
453 trivalent REE, which produced Ce-poor, HREE-rich minerals, and
454 hematitization of ilmenite attest to the high fO_2 values in the fluid. We infer that
455 the interaction of the hydrothermal system with external meteoric fluids led to a
456 sudden drop in temperature and CO_2 - H_2O immiscibility, which triggered REE
457 supersaturation and the deposition of nanocrystalline Ce-poor, Nd-Y-rich
458 bastnäsite-(La) and cerianite in the Zhaibei granites. This process has
459 far-reaching implications for the understanding of precursors and prerequisite
460 conditions to the development of HREE-rich IAD. Nanomineralization of the
461 type described in the present contribution could be a “missing link” between
462 magmatic REE hosts, which have low solubility in fluids, and ion-exchangeable

463 phases in the weathering profile. The polycrystalline nano-aggregates of REE
464 minerals are clearly more susceptible to weathering than primary monazite,
465 zircon or apatite (Fu et al. 2019). A detailed mineralogical study of precursor
466 igneous rocks is thus essential for constraining the HREE exploration potential
467 of IAD and for developing a comprehensive REE metallogenic model for these
468 deposits.

469

470

ACKNOWLEDGEMENTS AND FUNDING

471 We thank Bin Wu and Zhenyu Chen for mineral analyses. Zheng Zhao,
472 Yan Li, Ming Tang and Jin Liu are gratefully acknowledged for their assistance
473 in the field and data discussions. We are grateful to Daniel E. Harlov for
474 handling this manuscript and two anonymous reviewers for their constructive
475 comments. This research was supported financially by the National Natural
476 Science Foundation of China (41825008) and Guangxi Natural Science
477 Foundation (2020GXNSFGA297003). MS acknowledges support from the
478 UK-RI Natural Environment Research Council grant NE/V008935/1. J.K. was
479 supported by the Czech Science Foundation GACR EXPRO (grant number
480 19-29124X).

481

482

REFERENCES CITED

483 Bakker, R.J. (1997) Clathrates: Computer programs to calculate fluid inclusion

484 VX properties using clathrate melting temperatures. *Computers &*
485 *Geosciences*, 23, 1-18.

486 Balaram, V. (2019) Rare earth elements: A review of applications, occurrence,
487 exploration, analysis, recycling, and environmental impact. *Geoscience*
488 *Frontiers*, 10, 1285-1303.

489 Banfield, J.F., Welch, S.A., Zhang, H.Z., Ebert, T.T., and Penn, R.L. (2000)
490 Aggregation-based crystal growth and microstructure development in
491 natural iron oxyhydroxide biomineralization products. *Science*, 289,
492 751-754.

493 Bao, Z., and Zhao, Z. (2008) Geochemistry of mineralization with
494 exchangeable REY in the weathering crusts of granitic rocks in South
495 China. *Ore Geology Reviews*, 33, 519-535.

496 Bernhardt, D., and Reilly, I.I.J.F. (2020) Mineral Commodity Summaries 2020.
497 US Geological Survey.

498 Bodnar, R. (1993) Revised equation and table for determining the freezing
499 point depression of H₂O-NaCl solutions. *Geochimica et Cosmochimica*
500 *Acta*, 57, 683-684.

501 Boneschanscher, M.P., Evers, W.H., Geuchies, J.J., Altantzis, T., Goris, B.,
502 Rabouw, F.T., van Rossum, S.A.P., van der Zant, H.S.J., Siebbeles, L.D.A.,
503 Van Tendeloo, G., Swart, I., Hilhorst, J., Petukhov, A.V., Bals, S., and
504 Vanmaekelbergh, D. (2014) Long-range orientation and atomic

505 attachment of nanocrystals in 2D honeycomb superlattices. *Science*, 344,
506 1377-1380.

507 Borst, A.M., Smith, M.P., Finch, A.A., Estrade, G., Villanova-de-Benavent, C.,
508 Nason, P., Marquis, E., Horsburgh, N.J., Goodenough, K.M., Xu, C.,
509 Kynicky, J., and Geraki, K. (2020) Adsorption of rare earth elements in
510 regolith-hosted clay deposits. *Nature Communications*, 11, 4386.

511 Bowers, T.S., and Helgeson, H.C. (1983) Calculation of thermodynamic and
512 geochemical consequences of non-ideal mixing in the system
513 H₂O-CO₂-NaCl on phase relations in geologic systems: equation of state
514 for H₂O-CO₂-NaCl fluids at high pressures and temperatures. *Geochimica
515 et Cosmochimica Acta*, 47, 1247-1275.

516 Bray, A.J. (2002) Theory of phase-ordering kinetics. *Advances in Physics*, 51,
517 481-587.

518 Brock, T.D. (1985) Life at high temperatures. *Science*, 230, 132-138.

519 Burnham, A.D., and Berry, A.J. (2014) The effect of oxygen fugacity, melt
520 composition, temperature and pressure on the oxidation state of cerium in
521 silicate melts. *Chemical Geology*, 366, 52-60.

522 Burton, W.K., Cabrera, N., and Frank, F.C. (1951) The growth of crystals and
523 the equilibrium structure of their surfaces. *Philosophical Transactions of
524 the Royal Society of London. Series A, Mathematical and Physical
525 Sciences*, 243, 299-358.

526 Carrigan, C.R. (1986) A two-phase hydrothermal cooling model for shallow
527 intrusions. *Journal of volcanology and geothermal research*, 28, 175-192.

528 Chakhmouradian, A.R., Reguir, E.P., Zaitsev, A.N., Couëslan, C., Xu, C.,
529 Kynicky, J., Mumin, A.H., and Yang, P. (2017) Apatite in carbonatitic rocks:
530 Compositional variation, zoning, element partitioning and petrogenetic
531 significance. *Lithos*, 274-275, 188-213.

532 Chen, S., Zhang, Y., Zhang, X., Zhao, J., Zhao, Z., Su, X., Hua, Z., Zhang, J.,
533 Cao, J., Feng, J., Wang, X., Li, X., Qi, J., Li, J., and Gao, P. (2020)
534 General decomposition pathway of organic–inorganic hybrid perovskites
535 through an intermediate superstructure and its suppression mechanism.
536 *Advanced Materials*, 32, 2001107.

537 Chueh, P.L., and Prausnitz, J.M. (1967) Vapor-liquid equilibria at high
538 pressures. Vapor-phase fugacity coefficients in nonpolar and
539 quantum-gas mixtures. *Industrial & Engineering Chemistry Fundamentals*,
540 6, 492-498.

541 Cölfen, H., and Antonietti, M. (2008) Mesocrystals and nonclassical
542 crystallization. Ch. 9 (Wiley).

543 Cui, H., Zhong, R., Xie, Y., Yuan, X., Liu, W., Brugger, J., and Yu, C. (2020)
544 Forming sulfate-and REE-rich fluids in the presence of quartz. *Geology*,
545 48, 145-148.

546 De Yoreo, J.J., Gilbert, P.U.P.A., Sommerdijk, N.A.J.M., Penn, R.L., Whitlam,

547 S., Joester, D., Zhang, H.Z., Rimer, J.D., Navrotsky, A., Banfield, J.F.,
548 Wallace, A.F., Michel, F.M., Meldrum, F.C., Cölfen, H., and Dove, P.M.
549 (2015) Crystallization by particle attachment in synthetic, biogenic, and
550 geologic environments. *Science*, 349, aaa6760.

551 Estrade, G., Marquis, E., Smith, M., Goodenough, K., and Nason, P. (2019)
552 REE concentration processes in ion adsorption deposits: evidence from
553 the Ambohimirahavavy alkaline complex in Madagascar. *Ore Geology*
554 *Reviews*, 112, 103027.

555 Fu, W., Li, X., Feng, Y., Feng, M., Peng, Z., Yu, H., and Lin, H. (2019) Chemical
556 weathering of S-type granite and formation of Rare Earth Element
557 (REE)-rich regolith in South China: Critical control of lithology. *Chemical*
558 *Geology*, 520, 33-51.

559 Gulley, A.L., Nassar, N.T., and Xun, S. (2018) China, the United States, and
560 competition for resources that enable emerging technologies.
561 *Proceedings of The National Academy of Sciences* ,115, 4111-4115.

562 Hammersley, A.P. (1997) FIT2D: An Introduction and Overview: European
563 Synchrotron Radiation Facility Internal Report ESRF97HA02T, 68, 58.

564 Harlov, D.E., and Förster, H.J. (2003) Fluid-induced nucleation of (Y+
565 REE)-phosphate minerals within apatite: Nature and experiment. Part II.
566 Fluorapatite. *American Mineralogist*, 88, 1209-1229.

567 Harlov, D.E. (2015) Apatite: a fingerprint for metasomatic processes. *Elements*,

568 11, 171-176.

569 He, C., Xu, C., Zhao, Z., Kynicky, J., Song, W.L., and Wang, L.Z. (2017)
570 Petrogenesis and mineralization of REE-rich granites in Qingxi and
571 Guanxi, Nanling region, South China. *Ore Geology Reviews*, 81, 309-325.

572 Hochella Jr, M.F., Kasama, T., Putnis, A., Putnis, C.V., and Moore, J.N. (2005)
573 Environmentally important, poorly crystalline Fe/Mn hydrous oxides:
574 ferrihydrite and a possibly new vernadite-like mineral from the Clark Fork
575 River Superfund Complex. *American Mineralogist*, 90, 718-724.

576 Huang, F., Gilbert, B., Zhang, H.H., and Banfield, J.F. (2004) Reversible,
577 surface-controlled structure transformation in nanoparticles induced by an
578 aggregation state. *Physical Review Letters*, 92, 155501.

579 Ivanov, V.K., Fedorov, P.P., Baranchikov, A.Y., and Osiko, V.V. (2014) Oriented
580 attachment of particles: 100 years of investigations of non-classical crystal
581 growth. *Russian Chemical Reviews*, 83, 1204-1222.

582 Janots, E., Bernier, F., Brunet, F., Munoz, M., Trcera, N., Berger, A., and
583 Lanson, M. (2015) Ce (III) and Ce (IV)(re) distribution and fractionation in
584 a laterite profile from Madagascar: insights from in situ XANES
585 spectroscopy at the Ce LIII-edge. *Geochimica et Cosmochimica Acta*, 153,
586 134-148.

587 Jeon, S., Heo, T., Hwang, S.Y., Ciston, J., Bustillo, K.C., Reed, B.W., Ham,
588 J.M., Kang, S.S., Kim, S.G., Lim, J., Lim, K., Kim, J.S., Kang, M.H., Bloom,

589 R.S., Hong, S., Kim, K., Zettl, A., Kim, W.Y., Ercius, P., Park, J., and Lee,
590 W.C. (2021) Reversible disorder-order transitions in atomic crystal
591 nucleation. *Science*, 371, 498-503.

592 Kalvig, P., and Machacek, E. (2018) Examining the rare-earth elements (REE)
593 supply-demand balance for future global wind power scenarios. *GEUS*
594 *Bulletin*, 41, 87-90.

595 Kashchiev, D. (2003) Thermodynamically consistent description of the work to
596 form a nucleus of any size. *The Journal of Chemical Physics*, 118,
597 1837-1851.

598 Kelley, K.A., and Cottrell, E. (2012) The influence of magmatic differentiation
599 on the oxidation state of Fe in a basaltic arc magma. *Earth and Planetary*
600 *Science Letters*, 329, 109-121.

601 Li, D.S., Nielsen, M.H., Lee, J.R.I., Frandsen, C., Banfield, J.F., and De Yoreo,
602 J.J. (2012) Direction-specific interactions control crystal growth by
603 oriented attachment. *Science*, 336, 1014-1018.

604 Li, X.H., Chen, Z.G., Li, D.Y., and Li, W.X. (2003) Jurassic
605 gabbro-granite-syenite suites from southern Jiangxi Province, SE China:
606 age, origin, and tectonic significance. *International Geology Review*, 45,
607 898-921.

608 Li, X.Y., Chi, G.X., Zhou, Y.Z., Deng, T., and Zhang, J.R. (2017) Oxygen
609 fugacity of Yanshanian granites in South China and implications for

610 metallogeny. *Ore Geology Reviews*, 88, 690-701.

611 Li, Z.X., and Li, X.H. (2007) Formation of the 1300-km-wide intracontinental
612 orogen and postorogenic magmatic province in Mesozoic South China: a
613 flat-slab subduction model. *Geology*, 35, 179-182.

614 Liu, S.F., Gurnis, M., Ma, P.F., and Zhang, B. (2017) Reconstruction of
615 northeast Asian deformation integrated with western Pacific plate
616 subduction since 200 Ma. *Earth-Science Reviews*, 175, 114-142.

617 Mao, J.W., Xie, G.Q., Guo, C.L., Yuan, S.D., Cheng, Y.B., and Chen, Y.C.
618 (2008) Spatial temporal distribution of Mesozoic ore deposits in South
619 China and their metallogenic settings. *Geological Journal of China
620 Universities*, 14, 510–526.

621 Martin L.Y.H., Zhao, W.W., and Zhou, M.F. (2017) Nature of parent rocks,
622 mineralization styles and ore genesis of regolith-hosted REE deposits in
623 South China: an integrated genetic model. *Journal of Asian Earth
624 Sciences*, 148, 65-95.

625 Martin L.Y.H., and Zhou, M.F. (2020) The role of clay minerals in formation of
626 the regolith-hosted heavy rare earth element deposits. *American
627 Mineralogist*, 105, 92-108.

628 Migdisov A., Williams-Jones, A.E., Brugger, J., and Caporuscio, F.A. (2016)
629 Hydrothermal transport, deposition, and fractionation of the REE:
630 Experimental data and thermodynamic calculations. *Chemical Geology*,

631 439, 13-42.

632 Monshi, A., Foroughi, M.R., and Monshi, M.R. (2012) Modified Scherrer
633 equation to estimate more accurately nano-crystallite size using XRD.
634 World Journal of Nano Science and Engineering, 2, 154-160.

635 Nielsen, M.H., Li, D.S., Zhang, H.Z., Aloni, S., Han, T.Y.J., Frandsen, C., Seto,
636 J., Banfield, J.F., Cölfen, H., and De Yoreo, J.J. (2014) Investigating
637 processes of nanocrystal formation and transformation via liquid cell TEM.
638 Microscopy and Microanalysis, 20, 425-436.

639 Penn, R.L., and Banfield, J.F. (1999) Morphology development and crystal
640 growth in nanocrystalline aggregates under hydrothermal conditions:
641 insights from titania. *Geochimica et Cosmochimica Acta*, 63, 1549-1557.

642 Penn, R.L., Zhu, C., Xu, H., and Veblen, D.R. (2001) Iron oxide coatings on
643 sand grains from the Atlantic coastal plain: high-resolution transmission
644 electron microscopy characterization. *Geology*, 29, 843-846.

645 Prameswara, G., Trisnawati, I., Mulyono, P., Prasetya, A., and Petrus, H.T.B.M.
646 (2021) Leaching behaviour and kinetic of light and heavy rare earth
647 elements (REE) from zircon tailings in Indonesia. *The Journal of the
648 Minerals, Metals & Materials Society*, 73, 988-998.

649 Rice, S.B., Koo, J.Y., Disko, M.M., and Treacy, M.M.J. (1990) On the imaging
650 of Pt atoms in zeolite frameworks. *Ultramicroscopy*, 34, 108-118.

651 Sanematsu, K., Kon, Y., Imai, A., Watanabe, K., and Watanabe, Y. (2013)

652 Geochemical and mineralogical characteristics of ion-adsorption type
653 REE mineralization in Phuket, Thailand. *Mineralium Deposita*, 48,
654 437-451.

655 Scheifele, B., Saika-Voivod, I., Bowles, R.K., and Poole, P.H. (2013)
656 Heterogeneous nucleation in the low-barrier regime. *Physical Review E*,
657 87, 042407.

658 Shannon, R.D. (1976) Revised effective ionic radii and systematic studies of
659 interatomic distances in halides and chalcogenides. *Acta*
660 *Crystallographica Section A: Crystal Physics, Diffraction, Theoretical and*
661 *General Crystallography*, 32, 751-767.

662 Soare, L.C., Bowen, P., Lemaitre, J., and Hofmann, H. (2006) Precipitation of
663 nanostructured copper oxalate: substructure and growth mechanism. *The*
664 *Journal of Physical Chemistry B*, 110, 17763-17771.

665 Sun, F., Xu, X., Zou, H., and Xia, Y. (2015) Petrogenesis and magmatic
666 evolution of ~130 Ma A-type granites in Southeast China. *Journal of Asian*
667 *Earth Sciences*, 98, 209-224.

668 Wallace, A.F., Hedges, L.O., Fernandez-Martinez, A., Raiteri, P., Gale, J.D.,
669 Waychunas, G.A., Whitlam, S., Banfield, J.F., and De Yoreo, J.J. (2013)
670 Microscopic evidence for liquid-liquid separation in supersaturated CaCO₃
671 solutions. *Science*, 341, 885-889.

672 Wang, L.Z., Xu, C., Zhao, Z., Song, W.L., and Kynicky, J. (2015) Petrological

673 and geochemical characteristics of Zhaibei granites in Nanling region,
674 Southeast China: implications for REE mineralization. *Ore Geology*
675 *Reviews*, 64, 569-582.

676 Wang, R.C., Xie, L., Lu, J.J., Zhu, J.C., and Chen, J. (2017) Diversity of
677 Mesozoic tin-bearing granites in the Nanling and adjacent regions, South
678 China: distinctive mineralogical patterns. *Science China Earth Sciences*,
679 60, 1909-1919.

680 Wang, Y., Fan, W., Zhang, G., and Zhang, Y. (2013) Phanerozoic tectonics of
681 the South China Block: key observations and controversies. *Gondwana*
682 *Research*, 23, 1273-1305.

683 Wilson, M.J. (2004) Weathering of the primary rock-forming minerals:
684 processes, products and rates. *Clay Minerals*, 39, 233-266.

685 Wood, S.A. (1990) The aqueous geochemistry of the rare-earth elements and
686 yttrium: 1. Review of available low temperature data for inorganic
687 complexes and the inorganic REE speciation of natural waters. *Chemical*
688 *Geology*, 82, 159-186.

689 Xiong, Y.L. (2015) Experimental Determination of Solubility of Cerianite (CeO₂)
690 in High Ionic Strength Solutions at Elevated Temperatures. An Analog to
691 Tetravalent Actinides (No. SAND2015-9186C). Sandia National
692 Lab.(SNL-NM), Albuquerque, NM (United States).

693 Xu, C., Kynický, J., Smith, M.P., Kopriva, A., Brtnický, M., Urubek, T., Yang,

694 Y.H., Zhao, Z., He, C., and Song, W.L. (2017) Origin of heavy rare earth
695 mineralization in South China. *Nature Communications*, 8, 1-7.

696 Yardley, B., and Bottrell, S. (1988) Immiscible fluids in metamorphism:
697 implications of two-phase flow for reaction history. *Geology*, 16, 199-202.

698 Zhang, A.C., Wang, S.Z., Tomioka, N., Lu, X.C., Ding, Z.Y., Ma, C., Wang, P.,
699 Chen, J.N., Xu, S., Gu, L.X., Bai, Y.Q., Li, Y., Sakamoto, N., and Wang,
700 R.C. (2019) An example of high-T, high-symmetry crystallization: spherical
701 (Mg, Fe)-oxides formed by particle attachment in the shocked Martian
702 meteorite Northwest Africa 7755. *American Mineralogist: Journal of Earth
703 and Planetary Materials*, 104, 150-157.

704 Zhang, J., Huang, F., and Lin, Z. (2010) Progress of nanocrystalline growth
705 kinetics based on oriented attachment. *Nanoscale*, 2, 18-34.

706 Zhou, B.X., Sun, T., Shen, W., Shu, L., and Niu, Y. (2006) Petrogenesis of
707 Mesozoic granitoids and volcanic rocks in South China: a response to
708 tectonic evolution. *Episodes*, 29, 26.

709 Zhou, Y., Liang, X., Wu, S., Cai, Y., Liang, X., Shao, T., Wang, C., Fu, J., and
710 Jiang, Y. (2015) Isotopic geochemistry, zircon U–Pb ages and Hf isotopes
711 of A-type granites from the Xitian W–Sn deposit, SE China: Constraints on
712 petrogenesis and tectonic significance. *Journal of Asian Earth Sciences*,
713 105, 122-139.

714

715 **Endnote:**

716 ¹Deposit item ##, Online Materials. Deposit items are free to all readers and
717 found on the MSA website, via the specific issue's Table of Contents (go to
718 <http://www.minsocam.org/MSA/AmMin/##>).

719

720 **FIGURE CAPTIONS**

721 **FIGURE 1.** Distribution of granites in southeastern China and the location of
722 the Zhaibei granite (modified after Wang et al. 2017).

723

724 **FIGURE 2.** Representative photomicrographs of minerals from the Zhaibei
725 granites. (a) As-yet unidentified phases "REE-1" and "REE-2" formed by
726 alteration of magmatic fluorapatite (Ap). (b) Ce-poor, Nd-Y-rich bastnäsite-(La)
727 [Bast (La)] in fractures cross-cutting K-feldspar (Kfs) and plagioclase (Pl). (c)
728 Encrustations of Ce-poor, Nd-Y-rich bastnäsite-(La) lining a cavity interstitial to
729 quartz (Q). (d) Hydrous Al-Fe-rich silicate at the contact between Ce-poor and
730 Nd-Y-rich bastnäsite-(La), biotite (Bt) and K-feldspar. (e) Veinlet of cerianite
731 intergrown with an unidentified hydrous Al-Fe-rich silicate. (f) Ilmenite (Ilm)
732 partially converted to hematite (Hem).

733

734 **FIGURE 3.** In-situ synchrotron radiation-induced X-ray diffraction analysis of
735 Ce-poor, Nd-Y-rich bastnäsite-(La) [Bast (La)]. (a) Location of the analyzed

736 area within a 75- μm circle; (b) X-ray diffraction pattern and diffraction rings.

737

738 **FIGURE 4.** High-angle annular dark-field scanning transmission electron
739 microscopy (HAADF STEM) image showing nanoparticles of Ce-poor,
740 Nd-Y-rich bastnäsite-(La) (a) and nano-scale compositional maps (b-g)
741 showing a uniform distribution of C, O, F, La, Nd and Y within the
742 nanoparticles.

743

744 **FIGURE 5.** HRTEM image of an irregular boundary between
745 submicrometer-sized particles and nanoparticles of Ce-poor, Nd-Y-rich
746 bastnäsite-(La).

747

748 **FIGURE 6.** HRTEM images of Ce-poor, Nd-Y-rich bastnäsite-(La). (a)
749 Nanoparticles of randomly aggregated Ce-poor, Nd-Y-rich bastnäsite-(La);
750 their FFT pattern shows diffraction rings. (b) Nanoparticles partially aggregated
751 by oriented attachment, with FFT pattern exhibiting diffraction spots and rings.
752 (c) Advanced stage of nanoparticle assembly, with some local misalignment in
753 particle orientation (red circles); note regular diffraction spots in the FFT
754 pattern. (d) Aggregated nanoparticles showing a near-perfect alignment and a
755 well-defined diffraction pattern.

756

757 **FIGURE 7.** Representative photomicrographs of fluid inclusions in quartz. (a)
758 CO₂-H₂O inclusions (Type I) with various gas/liquid filling ratios. (b)
759 Three-phase CO₂-H₂O type inclusions. (c) Calcite daughter crystal (Cal) in a
760 fluid inclusion. (d) CO₂-rich inclusions coexisting with aqueous (Type II) fluid
761 inclusions.

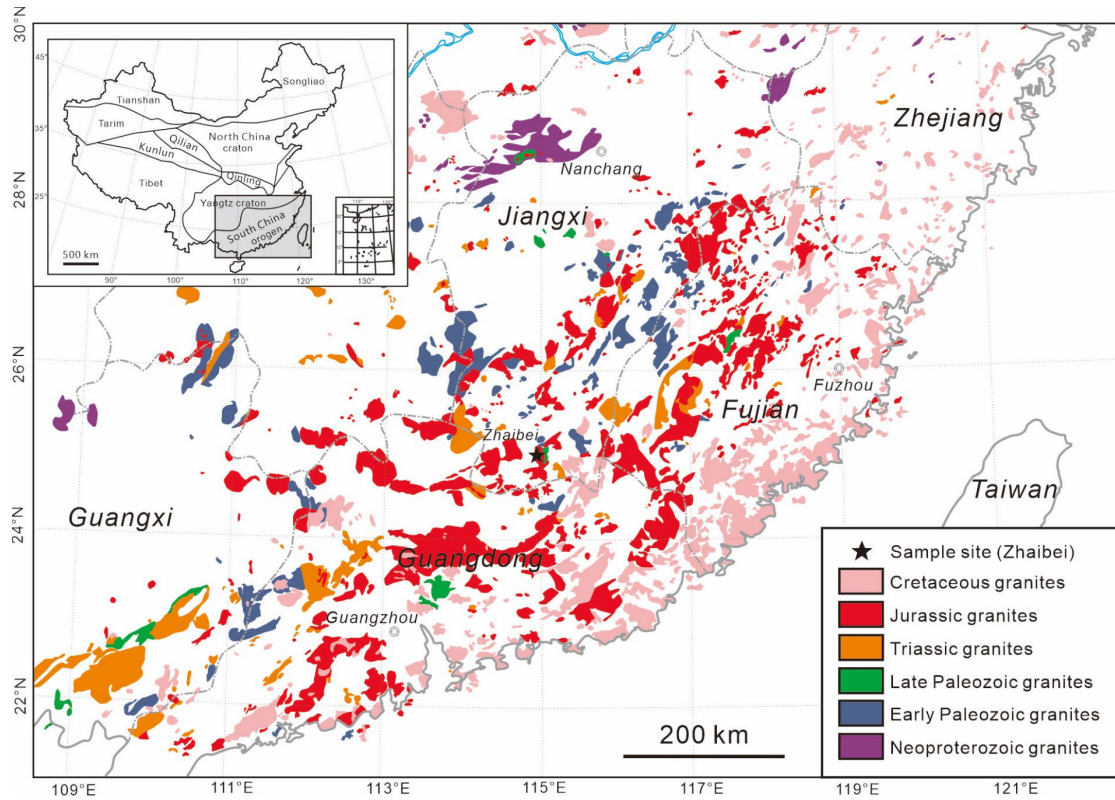


Figure 1. Distribution of granites in Southeast China and the location of Zhaibei granite (modified after Wang et al., 2017).

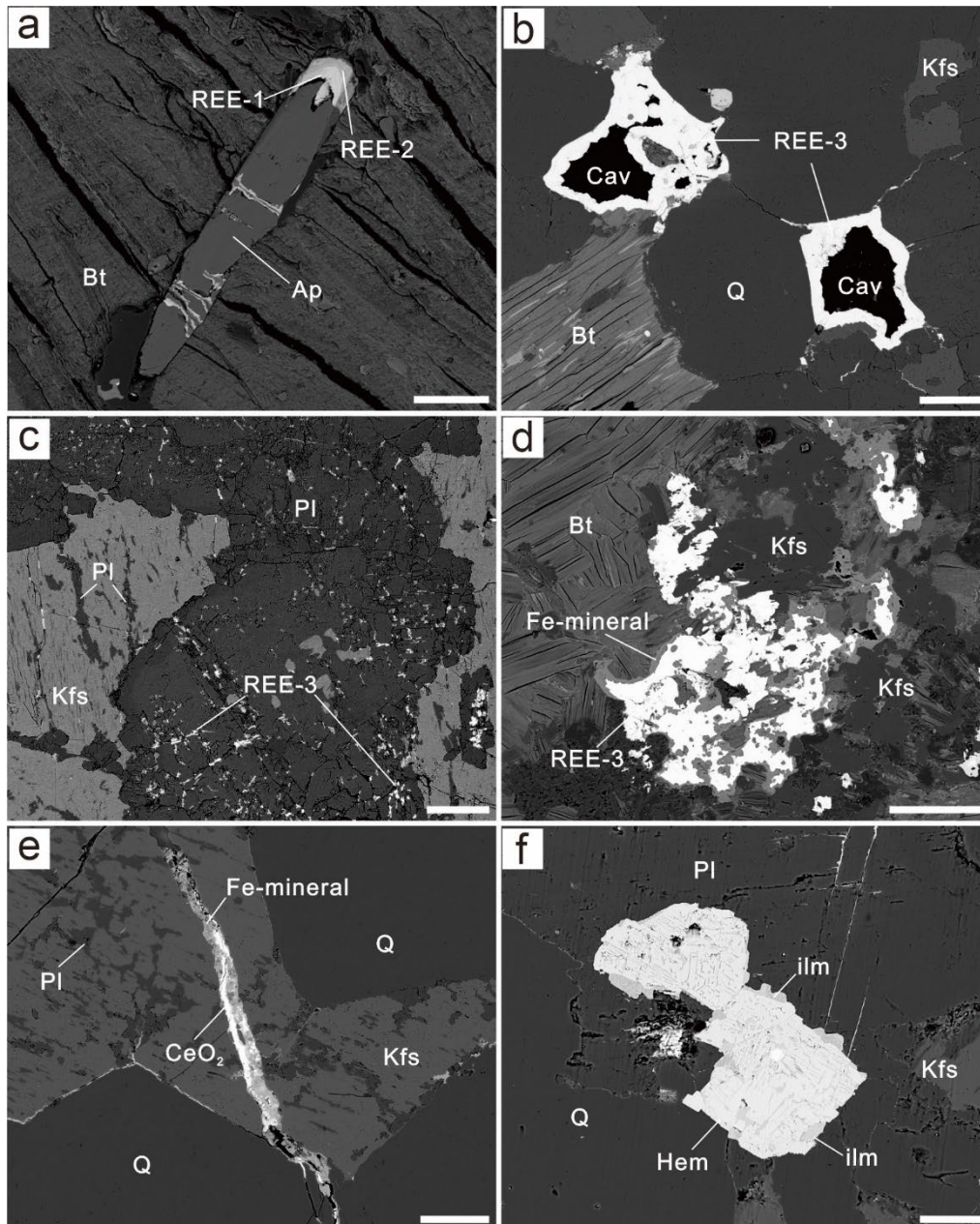


Figure 2. Representative photomicrographs of minerals from the Zhaibei granites. (a) As-yet unidentified phases “REE-1” and “REE-2” formed by alteration of magmatic fluorapatite (Ap). (b) Ce-poor, Nd-Y-rich bastnäsite-(La) [Bast (La)] in fractures cross-cutting K-feldspar (Kfs) and plagioclase (Pl). (c) Encrustations of Ce-poor, Nd-Y-rich bastnäsite-(La) lining a cavity interstitial to quartz (Q). (d) Hydrous Al-Fe-rich silicate at the contact between Ce-poor and Nd-Y-rich bastnäsite-(La), biotite (Bt), and K-feldspar. (e) Veinlet of cerianite intergrown with an unidentified hydrous Al-Fe-rich silicate. (f) Ilmenite (Ilm) partially converted to hematite (Hem).

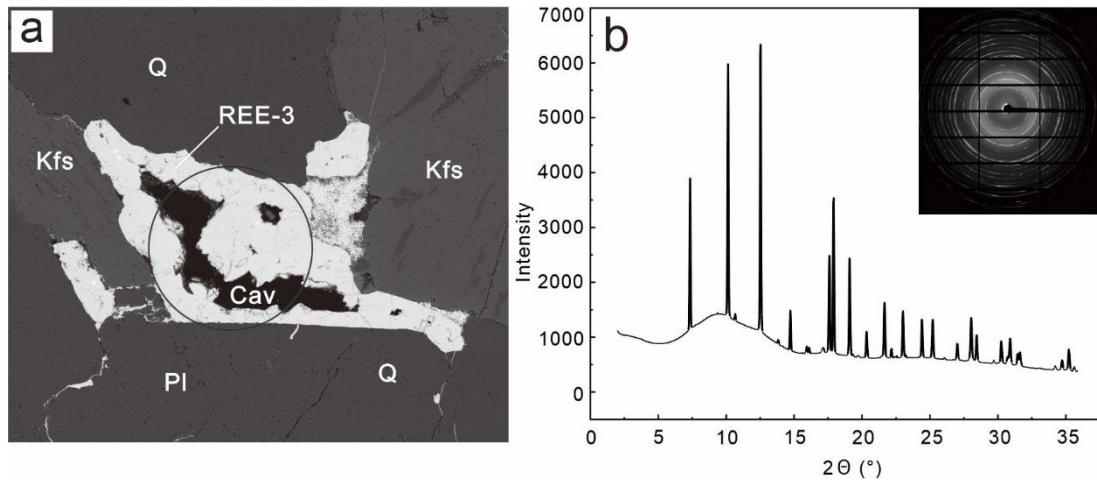


Figure 3. In situ synchrotron radiation-induced X-ray diffraction analysis of Ce-poor, Nd-Y-rich bastnäsite-(La) [Bast (La)]. (a) Location of the analyzed area within a 75 μm circle. (b) X-ray diffraction pattern and diffraction rings.

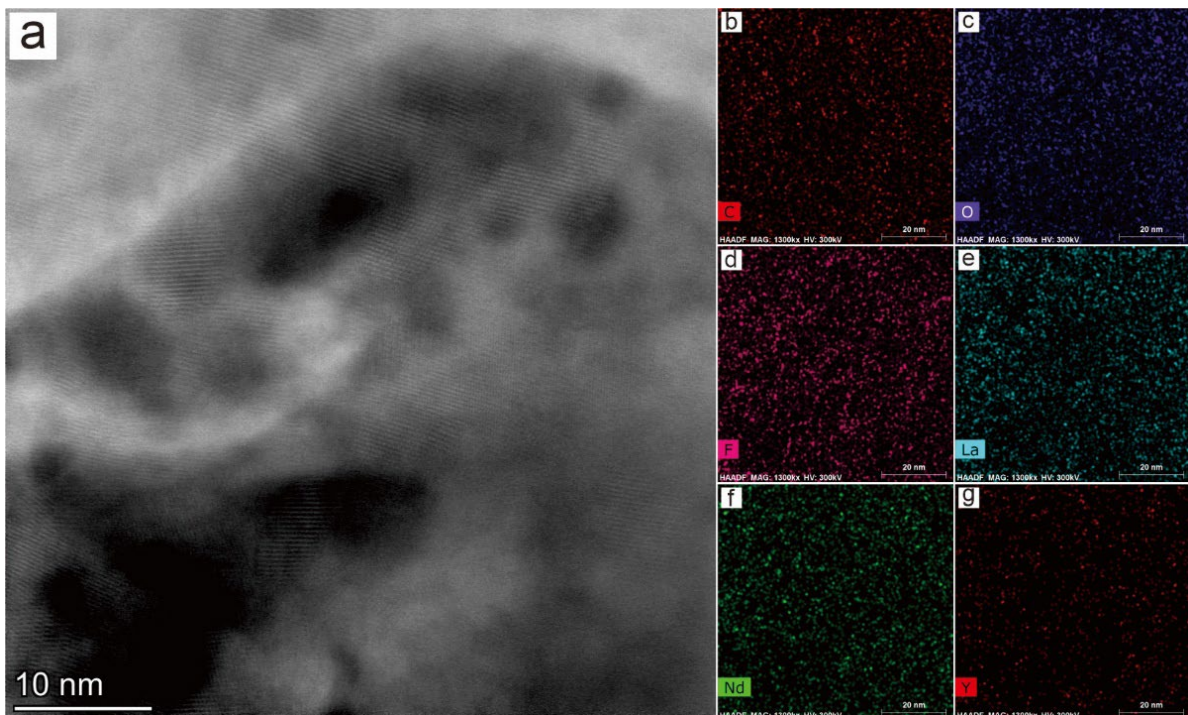


Figure 4. High-angle annular dark-field scanning transmission electron microscopy (HAADF STEM) image showing nanoparticles of Ce-poor, Nd-Y-rich bastnäsite-(La) (**a**) and nanoscale compositional maps (**b-g**) showing a uniform distribution of C, O, F, La, Nd, and Y within the nanoparticles.

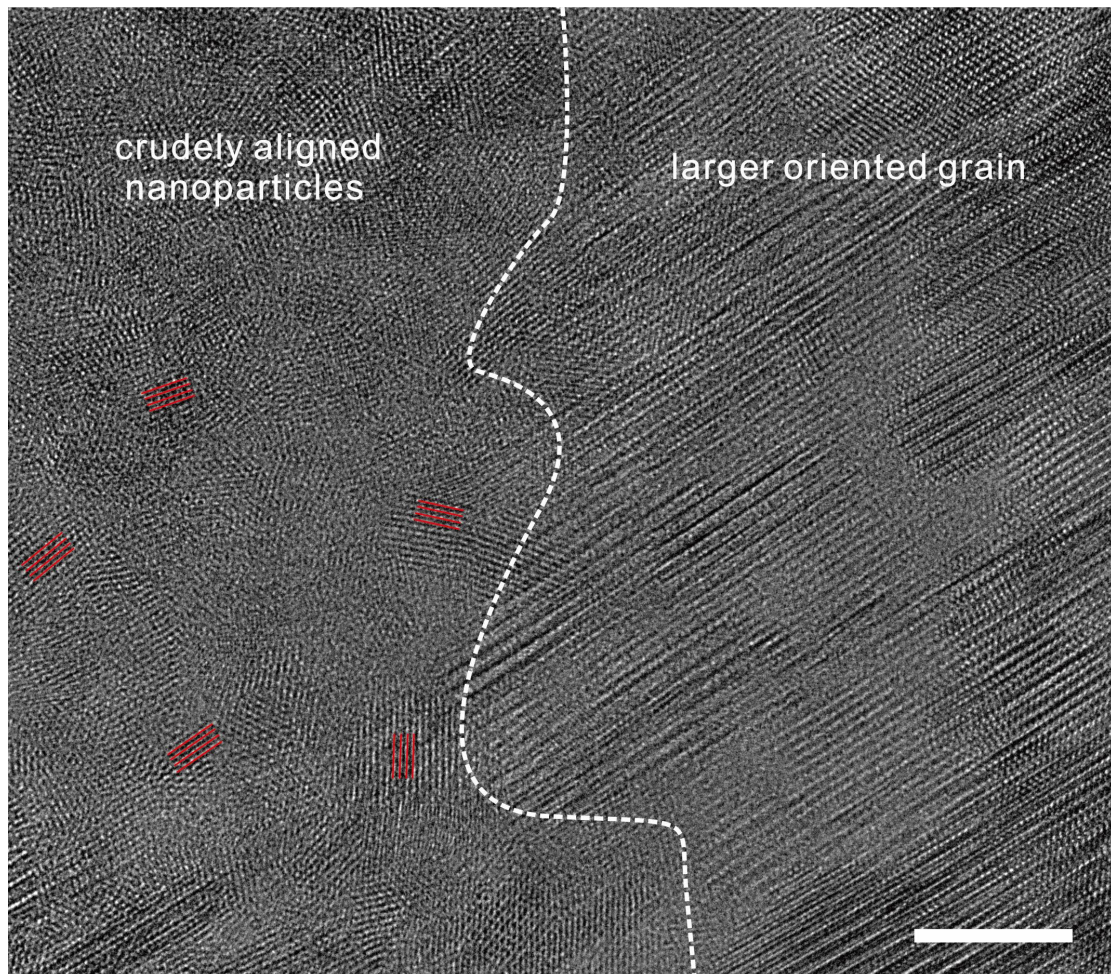


Figure 5. HRTEM image of an irregular boundary between submicrometer-sized particles and nanoparticles of Ce-poor, Nd-Y-rich bastnäsite-(La).

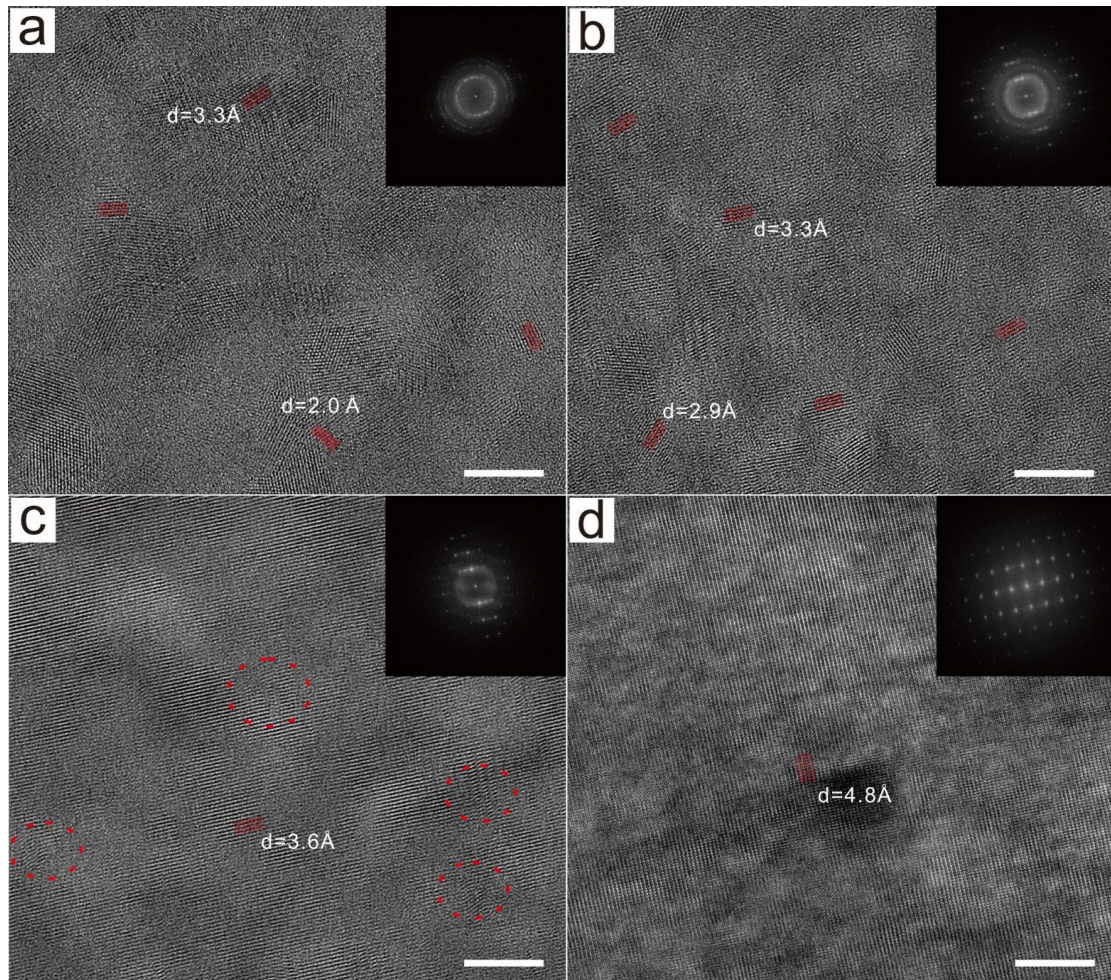


Figure 6. HRTEM images of Ce-poor, Nd-Y-rich bastnäsite-(La). **(a)** Nanoparticles of randomly aggregated Ce-poor, Nd-Y-rich bastnäsite-(La). Their FFT pattern shows diffraction rings. **(b)** Nanoparticles partially aggregated by oriented attachment with FFT pattern exhibiting diffraction spots and rings. **(c)** Advanced stage of nanoparticle assembly with some local misalignment in particle orientation (red circles). Note regular diffraction spots in the FFT pattern. **(d)** Aggregated nanoparticles showing a near-perfect alignment and a well-defined diffraction pattern.

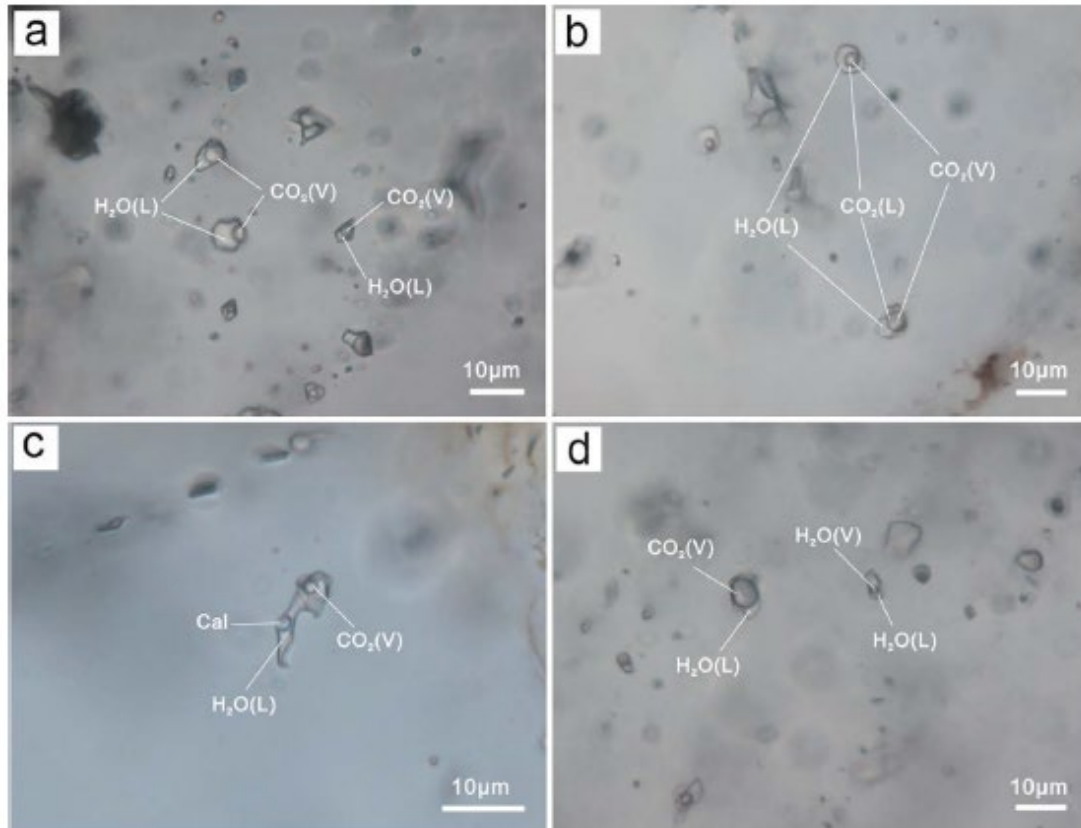


Figure 7. Representative photo-micrographs of fluid inclusions in quartz. **(a)** CO_2 - H_2O inclusions (Type I) with various gas/liquid filling ratios. **(b)** Three-phase CO_2 - H_2O type inclusions. **(c)** Calcite daughter crystal (Cal) in a fluid inclusion. **(d)** CO_2 - rich inclusions coexisting with aqueous (Type II) fluid inclusions.

Sample	1	2	3	4	5	6	7	8	9	10
P2O5	0.28	0.37	0.25	0.28	0.23	0.17	0.41	0.12	0.46	0.11
SiO2	0.02	0.03	0.06	0.04	0.02	0.05	0.13	0.08	bdl	0.01
ThO2	bdl	0.01	bdl	bdl	bdl	bdl	0.07	0.03	bdl	bdl
Al2O3	bdl	0.06	bdl	bdl	bdl	0.01	0.09	bdl	0.02	0.03
Y2O3	9.98	6.03	9.36	9.75	11.36	9.88	7.58	10.72	9.36	9.61
La2O3	29.62	29.67	29.45	29.44	30.01	29.29	29.51	29.68	30.06	29.71
Ce2O3	0.11	bdl	0.15	0.01	0.24	bdl	bdl	0.24	0.15	0.05
Pr2O3	5.11	6.24	5.24	5.29	4.71	5.07	5.13	5.11	4.83	5.15
Nd2O3	17.74	20.68	17.97	18.15	17	18.27	19.14	17.35	18.08	18.04
Sm2O3	3.75	4.25	3.88	3.8	3.76	3.99	4.01	3.97	4.03	4.06
Eu2O3	0.36	0.56	0.52	bdl	0.4	0.63	0.51	0.25	0.11	0.23
Gd2O3	2.97	2.46	3.06	2.84	3.41	3.08	2.74	3.1	3.13	3.1
Dy2O3	2.05	1.81	1.84	1.96	2.24	1.97	1.88	2.25	2.01	2.06
Ho2O3	1.48	1.57	1.26	1.09	1.24	1.12	1.48	1.41	1.55	1.57
Er2O3	0.11	0.26	bdl	0.06	0.27	bdl	0.27	0.16	0.37	0.32
Tm2O3	bdl	bdl	0.07	0.18	0.05	bdl	bdl	0.02	bdl	bdl
Yb2O3	0.54	0.44	0.39	bdl	0.02	0.19	0.23	0.23	0.19	0.3
CaO	0.52	0.52	0.54	0.53	0.48	0.55	0.51	0.66	0.47	0.54
FeO	bdl	0.02	0.05	0.08	0.1	0.05	bdl	0.01	bdl	0.01
K2O	bdl	0.02	0.01	0.01	0.01	0.05	0.01	0.03	bdl	0.01
F	5.66	5.56	5.24	6.04	5.13	5.68	8.02	4.98	4.77	5.52
CO2	21.27	20.94	21.12	21.04	21.72	21.31	20.81	21.71	21.22	21.32
H2O	1.67	1.65	1.83	1.44	2.01	1.65	0.47	2.06	2.09	1.73
O=F	-2.38	-2.34	-2.21	-2.54	-2.16	-2.39	-3.38	-2.10	-2.01	-2.32
Total	100.86	100.81	100.08	99.49	102.25	100.62	99.62	102.07	100.89	101.16
Formulas based on 1 cation										
P	0.008	0.011	0.007	0.008	0.007	0.005	0.012	0.003	0.013	0.003
Si	0.001	0.001	0.002	0.001	0.001	0.002	0.005	0.003	0	0
Th	0	0	0	0	0	0	0.001	0	0	0
Al	0	0.002	0	0	0	0	0.004	0	0.001	0.001
Y	0.183	0.112	0.173	0.181	0.204	0.181	0.142	0.193	0.172	0.176
La	0.376	0.383	0.377	0.378	0.374	0.373	0.382	0.371	0.382	0.378
Ce	0.001	0	0.002	0	0.003	0	0	0.003	0.002	0.001
Pr	0.064	0.08	0.066	0.067	0.058	0.064	0.066	0.063	0.061	0.065
Nd	0.218	0.258	0.223	0.226	0.205	0.225	0.24	0.21	0.222	0.222
Sm	0.045	0.051	0.046	0.046	0.044	0.047	0.049	0.046	0.048	0.048
Eu	0.004	0.007	0.006	0	0.005	0.007	0.006	0.003	0.001	0.003
Gd	0.034	0.029	0.035	0.033	0.038	0.035	0.032	0.035	0.036	0.035
Dy	0.023	0.02	0.021	0.022	0.024	0.022	0.021	0.025	0.022	0.023
Ho	0.016	0.017	0.014	0.012	0.013	0.012	0.017	0.015	0.017	0.017
Er	0.001	0.003	0	0.001	0.003	0	0.003	0.002	0.004	0.003
Tm	0	0	0.001	0.002	0.001	0	0	0	0	0
Yb	0.006	0.005	0.004	0	0	0.002	0.002	0.002	0.002	0.003
Ca	0.019	0.019	0.02	0.02	0.017	0.02	0.019	0.024	0.017	0.02
Fe	0	0.001	0.001	0.002	0.003	0.001	0	0	0	0
K	0	0.001	0	0	0	0.002	0	0.001	0	0
F	0.617	0.615	0.576	0.666	0.548	0.62	0.891	0.534	0.52	0.602
C	1.001	1	1.001	1.001	1.002	1.004	0.998	1.004	0.998	1.004
H	0.383	0.385	0.424	0.334	0.452	0.38	0.109	0.466	0.48	0.398

Table 1. Compositions (wt%) of Ce-poor, Nd-Y-rich bastnäsite-(La) in the Zhaibei granites. Bdl=below detection limit. CO2 in the mineral is calculated using charge balance method. H2O is calculated assuming a full (F,OH) site. bdl = below determination limits.

Sample	11	12	13	14	15	16	17	18	19	20
P2O5	0.06	0.15	1.38	0.45	0.12	bdl	0.03	0.04	0.06	0.35
SiO2	0.04	0.07	0.08	0.03	0.51	bdl	0.04	0.05	0.03	0.07
ThO2	bdl	0.05	bdl	bdl	bdl	bdl	bdl	bdl	bdl	bdl
Al2O3	bdl	0.04	bdl	0.01	0.06	bdl	0.01	bdl	bdl	0.02
Y2O3	10.21	7.45	12.92	9.85	10.73	8.1	8.07	8.55	8.6	8.49
La2O3	29.14	29.16	27.82	30.62	29.5	29.06	29.88	29.2	29.34	30.39
Ce2O3	0.07	0.04	bdl	bdl	bdl	0.01	bdl	bdl	bdl	bdl
Pr2O3	5.06	5.6	4.69	5.05	5.05	5.61	5.51	5.33	5.4	5.65
Nd2O3	17.82	20.02	16.1	18.31	17.48	19.68	20.05	20.25	19.46	19.13
Sm2O3	3.81	4.5	3.19	3.96	3.8	4.23	4.37	4.36	4.27	4.16
Eu2O3	0.25	0.24	0.02	0.56	0.28	0.68	0.52	0.73	0.71	0.49
Gd2O3	3.26	2.92	3.01	3.14	2.76	2.93	2.77	2.65	3.03	2.59
Dy2O3	2.1	1.73	2.36	2.05	2.43	1.89	1.87	1.81	1.95	1.84
Ho2O3	1.59	1.14	1.85	1.07	1.38	1.17	1.48	1.48	1.35	1.07
Er2O3	0.14	0.26	0.37	0.14	0.31	0.25	0.23	0.07	0.14	0.17
Tm2O3	bdl	bdl	bdl	bdl	bdl	bdl	bdl	bdl	bdl	bdl
Yb2O3	0.36	0.19	0.62	0.22	0.14	0.39	0.39	0.02	0.41	0.3
CaO	0.54	0.51	0.49	0.55	0.65	0.57	0.63	0.54	0.6	0.59
FeO	bdl	bdl	0.01	0.03	0.06	0.04	0.01	0.06	bdl	bdl
K2O	0.01	0.03	0.01	0.02	0.17	0.01	0.01	0.01	bdl	0.01
F	5.71	5.87	5.51	5.09	5.32	5.19	5.51	5.85	5.54	6.13
CO2	21.26	20.87	21.74	21.72	22.06	21.07	21.44	21.29	21.32	21.38
H2O	1.63	1.48	1.91	2.04	1.98	1.83	1.75	1.56	1.72	1.47
O=F	-2.41	-2.47	-2.32	-2.14	-2.24	-2.18	-2.32	-2.46	-2.33	-2.58
Total	100.65	99.85	101.76	102.77	102.55	100.53	102.25	101.39	101.6	101.72
Formulas based on 1 cation										
P	0.002	0.004	0.039	0.013	0.003	0	0.001	0.001	0.002	0.01
Si	0.001	0.002	0.003	0.001	0.017	0	0.001	0.002	0.001	0.002
Th	0	0	0	0	0	0	0	0	0	0
Al	0	0.002	0	0	0.002	0	0	0	0	0.001
Y	0.188	0.139	0.228	0.177	0.19	0.151	0.147	0.157	0.158	0.155
La	0.372	0.378	0.34	0.38	0.363	0.375	0.378	0.372	0.373	0.384
Ce	0.001	0.001	0	0	0	0	0	0	0	0
Pr	0.064	0.072	0.057	0.062	0.061	0.071	0.069	0.067	0.068	0.071
Nd	0.22	0.252	0.191	0.22	0.208	0.246	0.246	0.25	0.24	0.234
Sm	0.045	0.055	0.036	0.046	0.044	0.051	0.052	0.052	0.051	0.049
Eu	0.003	0.003	0	0.006	0.003	0.008	0.006	0.009	0.008	0.006
Gd	0.037	0.034	0.033	0.035	0.03	0.034	0.032	0.03	0.035	0.029
Dy	0.023	0.02	0.025	0.022	0.026	0.021	0.021	0.02	0.022	0.02
Ho	0.017	0.013	0.02	0.011	0.015	0.013	0.016	0.016	0.015	0.012
Er	0.002	0.003	0.004	0.001	0.003	0.003	0.002	0.001	0.002	0.002
Tm	0	0	0	0	0	0	0	0	0	0
Yb	0.004	0.002	0.006	0.002	0.001	0.004	0.004	0	0.004	0.003
Ca	0.02	0.019	0.017	0.02	0.023	0.021	0.023	0.02	0.022	0.022
Fe	0	0	0	0.001	0.002	0.001	0	0.002	0	0
K	0	0.001	0	0.001	0.007	0	0	0	0	0
F	0.625	0.653	0.578	0.542	0.561	0.574	0.598	0.639	0.605	0.664
C	1.004	1.003	0.985	0.999	1.004	1.006	1.005	1.005	1.004	1
H	0.375	0.347	0.422	0.458	0.439	0.426	0.402	0.361	0.395	0.336

Table 1. Continued

Table 2. Summary of fluid inclusion data from the Zhaibei granites

inclusion type	size(μm)	Tm CO ₂	Tm C	Th CO ₂	Tm	salinity (wt.%)	Th
L ₁ +L ₂ +V	8	-58.1°C	4.2°C	31.1°C		10.3	307°C-L
L ₁ +L ₂ +V	5	-57.6°C	4.1°C	30.89°C		10.4	313°C-L
L ₁ +L ₂ +V	7	-57.6°C	5.7°C	30.2°C		8.0	327°C-L
L ₁ +L ₂ +V	7	-57.6°C	5.1°C	31.1°C		8.9	339°C-L
L ₁ +L ₂ +V	9	-57.7°C	5.8°C	29.8°C		7.8	343°C-L
L ₁ +L ₂ +V	8	-58.3°C	8.2°C	28.1°C		3.5	349°C-G
L ₁ +L ₂ +V	9	-57.2°C	5.2°C	29.7°C		8.8	356°C-L
L ₁ +L ₃ +V	8	-57.8°C	4.9°C	30.5°C		9.2	356°C-L
L ₁ +L ₂ +V	7	-57.5°C	5.4°C	28.9°C		8.5	361°C-L
L ₁ +L ₂ +V	8	-57.4°C	3.5°C	30.67°C		11.3	362°C-G
L ₁ +L ₄ +V	6	-58.2°C	6.3°C	30.2°C		6.9	362°C-L
L ₁ +L ₂ +V	8	-58.2°C	4.9°C	31.1°C		9.2	372°C-L
L ₁ +L ₂ +V	9	-58.2°C	7.9°C	28.5°C		4.1	386°C-G
L+V	7				-7.3°C	10.9	168°C
L+V	9				-5.6°C	8.7	174°C
L+V	11				-6.3°C	9.6	182°C
L+V	9				-4.9°C	7.7	210°C
L+V	8				-4.8°C	7.6	211°C
L+V	14				-6.4°C	9.7	218°C
L+V	5				-5.9°C	9.1	220°C
L+V	6				-6.4°C	9.7	253°C
L+V	5				-6.1°C	9.3	276°C
L+V	10				-5.4°C	8.4	313°C
L+V	7				-5.3°C	8.3	326°C
L+V	6				-4.8°C	7.6	345°C
L+V	9				-5.8°C	8.9	347°C

CO₂ melting temperatures (Tm CO₂)

Clathrate melting temperatures (Tm C)

Partial homogenization temperatures (Th CO₂)

Ice-melting temperatures (Tm)

Homogenization temperatures (Th)

The letter behind homogenization temperatures represents the form of homogenization